The Astrophysical Journal, 975:88 (16pp), 2024 November 1 https://doi.org/10.3847/1538-4357/ad79f4

Follow-up Timing of 12 Pulsars Discovered in Commensal Radio Astronomy FAST Survey

D. Zhao[1,2,3,4], J. P. Yuan[1,2,3], N. Wang[1,2,3], D. Li[5,6,7], P. Wang[6,8], M. Y. Xue[6], W. W. Zhu[6,8], C. C. Miao[7], W. M. Yan[1,2,3], J. B. Wang[1,2,9], J. M. Yao[1,2,3], Q. D. Wu[1,2,3], S. Q. Wang[1,2,3], S. N. Sun[1,2,3], F. F. Kou[1,2,3], Y. T. Chen[6,10], S. J. Dang[11], Y. Feng[7], Z. J. Liu[11], X. L. Miao[6], L. Q. Meng[6], M. Yuan[6], C. H. Niu[6,12], J. R. Niu[6], L. Qian[6], S. Wang[13], X. Y. Xie[11], Y. F. Xiao[14], Y. L. Yue[6], S. P. You[11], X. H. Yu[11], R. S. Zhao[11], R. Yuen[1,2,3], X. Zhou[1,2,3], L. Zhang[6], M. Xie[13], Y. X. Li[15], Y. B. Wang[15], Z. K. Luo[15], Z. Y. Gan[15], Z. Y. Sun[15], M. M. Chi[15], and C. J. Wang[15]

[1] Xinjiang Astronomical Observatory, Chinese Academy of Sciences, 150 Science 1-Street, Urumqi, Xinjiang 830011, People's Republic of China; yuanjp@xao.ac.cn, na.wang@xao.ac.cn, dili@mail.tsinghua.edu.cn
[2] Key Laboratory of Radio Astronomy and Technology (Chinese Academy of Sciences), A20 Datun Road, Chaoyang District, Beijing, 100101, People's Republic of China
[3] Xinjiang Key Laboratory of Radio Astrophysics, 150 Science1-Street, Urumqi, Xinjiang 830011, People's Republic of China
[4] School of Physical Science and Technology, Xinjiang University, Urumqi, Xinjiang 830046, People's Republic of China
[5] Department of Astronomy, Tsinghua University, Beijing 100084, People's Republic of China
[6] National Astronomical Observatories, Chinese Academy of Sciences, A20 Datun Road, Chaoyang District, Beijing 100101, People's Republic of China
[7] Zhejiang Lab, Hangzhou, Zhejiang 311121, People's Republic of China
[8] Institute for Frontiers in Astronomy and Astrophysics, Beijing Normal University, Beijing 102206, People's Republic of China
[9] Institute of Optoelectronic Technology, Lishui University, Lishui 323000, People's Republic of China
[10] University of Chinese Academy of Sciences, Beijing 100049, People's Republic of China
[11] Guizhou Normal University, Guiyang 550001, People's Republic of China
[12] Institute of Astrophysics, Central China Normal University, Wuhan 430079, People's Republic of China
[13] School of Computer Science, Fudan University, Shanghai 200438, People's Republic of China
[14] GuiZhou University, Guizhou 550025, People's Republic of China
[15] Tencent Youtu Lab, Shanghai 201103, People's Republic of China
Received 2024 March 13; revised 2024 September 1; accepted 2024 September 10; published 2024 October 30

Abstract

We present phase-connected timing ephemerides, polarization pulse profiles, and Faraday rotation measurements of 12 pulsars discovered by the Five-hundred-meter Aperture Spherical radio Telescope (FAST) in the Commensal Radio Astronomy FAST Survey. The observational data for each pulsar span at least 1 yr. Among them, PSR J1840+2843 shows subpulse drifting, and five pulsars are detected to exhibit pulse nulling phenomena. PSR J0640−0139 and PSR J2031−1254 are isolated millisecond pulsars (MSPs) with stable spin-down rates ($\dot{P}$) of $4.8981(6) \times 10^{-20}$ s s^{-1} and $6.01(2) \times 10^{-21}$ s s^{-1}, respectively. Additionally, one pulsar (PSR J1602−0611) is in a neutron star−white dwarf (WD) binary system with an 18.23-day orbit and a companion of $\leqslant 0.65\,M_{\odot}$. PSR J1602−0611 has a spin period, companion mass, and orbital eccentricity that are consistent with the theoretical expectations for MSP−helium WD (He WD) systems. Therefore, we believe that it might be an MSP−He WD binary system. The locations of PSR J1751−0542 and PSR J1840+2843 on the $P - \dot{P}$ diagram are beyond the traditional death line. This indicates that FAST has discovered some low-$\dot{E}$ pulsars, contributing new samples for testing pulsar radiation theories. We estimated the distances of these 12 pulsars based on NE2001 and YMW16 electron density models, and our work enhances the data set for investigating the electron density model of the Galaxy.

Unified Astronomy Thesaurus concepts: Pulsars (1306); Radio pulsars (1353); Binary pulsars (153); Millisecond pulsars (1062)

1. Introduction

Radio pulsars are high-speed rotating neutron stars (NSs) that are observed with periodic radio pulses. Because of its ultrahigh density, strong magnetic field, and ultrafast rotation frequency, it has become a natural laboratory for extreme physics. Pulsars are used to study stellar evolution (T. M. Tauris et al. 2017) to constrain the equation of state of ultradense matter (J. M. Lattimer & M. Prakash 2001; F. Özel & P. Freire 2016) and to map the distribution of free electrons in our Galaxy (J. M. Cordes & T. J. W. Lazio 2002; J. M. Yao et al. 2017). The discovery of low spin-down energy loss rate ($\dot{E}$) pulsars provides the possibility to test radiation theory. In the magnetic dipole frame, the pulsar period (P) and period derivative $\dot{P}$ can be used to estimate the spin-down luminosity ($\dot{E}$), characteristic age (τ_c), and surface magnetic field (B_s) of a pulsar. The death line of a pulsar defines the boundary at which the pulsar ceases radio emissions. When the pulsar is below the death line, it is not expected to produce radio emission any longer (M. A. Ruderman & P. G. Sutherland 1975; K. Chen & M. Ruderman 1993; B. Zhang et al. 2000). By incorporating general relativistic frame dragging (J. Arons & E. T. Scharlemann 1979) and considering curvature radiation and inverse Compton scattering, B. Zhang et al. (2000) proposed the vacuum gap model and the space charge limited flow (SCLF) model. The detection low-$\dot{E}$ and long-period pulsars plays a crucial role in advancing our understanding of the radiation mechanisms inherent to pulsars.

Radio millisecond pulsars (MSPs) are very stable rotators that are characterized by short spin periods ($P < 20$ ms) and very small spin-down rates ($\dot{P} \sim 10^{-20}$ s s^{-1}). MSPs are believed to form in binary systems in which the pulsars gain mass and angular momentum from the companion during the accretion process (D. Bhattacharya & E. P. J. van den Heuvel 1991). They are thus recycled and spun up to milliseconds, and they exhibit high rotational stability, manifested as accurate clocks in the Universe. Their clock-like periodic pulses from binary pulsars can be used to determine their orbital dynamics with high precision. Excluding those MSPs in globular clusters, which may be formed through dynamic processes, all MSPs should be in binary systems. However, approximately 20% of MSPs are isolated in the Galactic field. E. P. J. van den Heuvel & J. van Paradijs (1988) and W. Kluzniak et al. (1988) proposed that the donor stars may have been ablated by the γ-rays and energetic particles emitted by the MSPs. H.-L. Chen et al. (2013) suggest that the evaporation timescale may be too long unless there is a very high evaporation efficiency ($\sim$0.1). L. Jiang et al. (2020a) proposed a new process to form isolated MSPs. When the central density of NSs rises above the quark deconstrained density, a phase transition (PT) from NSs to strange stars may occur, and a suitable kick could disrupt the binary. Depending on the presence or absence of a companion star, MSPs are divided into binary and isolated pulsars. For MSPs with stable rotation and very high timing accuracy, they can also constitute the pulsar timing array (PTA). The timing array can not only be used to study the basic physics of NSs but also be a unique tool to detect the ultra−low-frequency gravitational waves generated by galaxy mergers and study the basic characteristics of ultra−low-frequency gravitational waves (G. Agazie et al. 2023a, 2023c, 2023e, 2023b, 2023d, 2023f; EPTA Collaboration et al. 2023a, 2023b, 2023c; D. J. Reardon et al. 2023; H. Xu et al. 2023). MSPs and binary pulsars have provided an opportunity for studying the evolution of stellar and binary systems (D. Bhattacharya & E. P. J. van den Heuvel 1991; F. D'Antona & M. Tailo 2022; D. Belloni & M. R. Schreiber 2023; B. Wang et al. 2024).

Pulsars exhibit highly polarized radio emissions (A. G. Lyne & F. G. Smith 1968), and studying their polarization properties helps reveal the radiation mechanisms and the geometry of the emission regions. Their high linear polarization allows us to measure the Faraday rotation measure (RM), which aids in investigating the structure of the Galactic magnetic field (R. N. Manchester 1974; J. L. Han et al. 2006). Observations show that many pulsars exhibit an S-shaped variation in polarization position angle (PA), which can be described by the rotating vector model (RVM; V. Radhakrishnan & D. J. Cooke 1969), allowing us to derive the pulsar's geometric parameters (P. F. Wang et al. 2023). Circular polarization is usually weak and exhibits sense reversal when the line of sight passes through the core component of the profile (J. M. Rankin 1983). Additionally, some pulsars exhibit discontinuous changes in PA, sometimes with 90° jumps, known as orthogonal polarization modes (OPMs; R. N. Manchester et al. 1975; D. R. Stinebring et al. 1984; N. Primak et al. 2022). In this work, we measured the polarization information of 12 Commensal Radio Astronomy FAST Survey (CRAFTS) pulsars. The high sensitivity of FAST will facilitate a more detailed study of pulsar polarization profiles.

Pulse nulling is a unique phenomenon in pulsar emissions, characterized by the sudden disappearance of the pulse signal for a period of time (e.g., N. Wang et al. 2007; P. F. Wang et al. 2020). Although the phenomenon of pulse nulling has been detected for many years, its emission physics is still unclear. Several models have been proposed to explain the nulling phenomenon. A. Lyne et al. (2010) proposed that variations in relativistic plasma flow are the underlying reason for the absence of emission during a null. B. Bhattacharyya et al. (2010) proposed a partial shielding gap model. When the temperature of the polar cap reaches several thousand kelvin, the pulsar cannot emit pulse signals, showing the phenomenon of pulse nulling. J. L. Herfindal & J. M. Rankin (2007) suggested that the periodic nulling could be caused by a partially ignited subbeam carousel. T. Olszanski et al. (2022) propose that nulling may be due to the evolution of pair formation geometries producing core/cone emission and other emission effects. At present, it is not clear how the variations of pulsar surface magnetosphere affect the modulation of pulsar emission intensity. Through long-term observations, it is also possible to study the causes of nulling phenomena and determine whether there is periodic behavior.

The world's largest single-dish telescope, FAST (R. Nan 2006; R. Nan et al. 2011; L. Qian et al. 2020), has discovered over 800 pulsars through CRAFTS[16] (D. Li et al. 2018), GPPS[17] (J. L. Han et al. 2021), and the FAST Globular Cluster Pulsar Survey[18] (Z. Pan et al. 2021). It is expected that these surveys will discover more MSPs in the future, making a significant contribution to this population. Among them, CRAFTS discovered over 200 pulsars,[19] including the first discoveries from FAST (Zhang et al. 2019; Qian and Pan et al. 2019) as well as 40 ms pulsars (P. Wang et al. 2021; Q. D. Wu et al. 2023a; C. C. Miao et al. 2023), over 20 binary star systems (M. Cruces et al. 2021; C. C. Miao et al. 2023), 1 DNS system candidate (Q. D. Wu et al. 2023b), 1 confirmed DNS system (D. Zhao et al. 2024), and 1 high-energy young pulsar with a γ-ray counterpart (P. Wang et al. 2021). A. D. Cameron et al. (2020) reported the timing analysis of 11 isolated pulsars found in CRAFTS. The work lays the foundation for future efforts of CRAFTS. M. Cruces et al. (2021) reported the timing analysis results of 10 pulsars found in the commissioning phase of FAST, one of which is a binary star. This work indicates that the pulsar survey could enrich the pulsar population and improve the electron density model of the Galaxy. C. C. Miao et al. (2023) reported 12 MSPs discovered with the FAST telescope in the CRAFTS. Eleven out of the 12 pulsars are in NS−helium white dwarf (He WD) binary systems, having companion masses consistent with the prediction of T. M. Tauris & G. J. Savonije (1999) for MSPs. Q. D. Wu et al. (2023a) reported 24 pulsars discovered with FAST in CRAFTS and suggest that electron density models need updates for higher Galactic latitude regions. Compared to pulsars discovered by other telescopes, CRAFTS can detect fainter and farther pulsars.

In this work, we report the timing results of 12 pulsars in FAST's CRFATS, including 9 isolated normal pulsars and 3 MSPs (2 isolated MSPs, PSR J0640−0139 and PSR J2031 −1254, and 1 binary, PSR J1602−0611). In Section 2, we describe our observation setting and data reduction procedures. We provide the results of follow-up timing observations in Section 3. Our summary of the results is presented in Section 4.

[16] http://crafts.bao.ac.cn
[17] http://zmtt.bao.ac.cn/GPPS/
[18] https://fast.bao.ac.cn/cms/article/65/
[19] doi.org/10.57760/sciencedb.Fastro.00003

2. Observations and Data Processing

These 12 pulsars were discovered by the NAOC-Tencent collaboration through the CRAFTS program (D. Li et al. 2018; M. Xie et al. 2022) and are regularly monitored by FAST. The 19-beam receiver has an effective bandwidth of 400 MHz from 1050 to 1450 MHz (P. Jiang et al. 2020b). The sampling rate of the observation is 49.152 μs. The observation data are recorded with full Stokes in the pulsar search mode. Each pulsar observation starts with a 40 s calibration noise diode for polarization calibration, with dish pointing at a sky region 10′ offset from the source. Therefore, after deducting the time needed for antenna slew, the integration time for each pulsar is 240 s per epoch.

Unlike known pulsars, these newly discovered pulsars do not have ephemerides available to predict the arrival time of pulses. Therefore, we first use the pulsar search analysis software PRESTO[20] (S. Ransom 2011) to confirm the initial spin period (P) and dispersion measures (DMs) of the new pulsars. For pulsars in binary systems, the apparent spin period and spin period derivative will significantly vary between epochs. From the initial few months of follow-up observations, we confirm that only one pulsar is in a binary system, and the other pulsars are isolated normal pulsars and MSPs. For the pulsars in binary systems, the initial ephemerides needs to not only contain coordinates, estimated spin frequency (ν), estimated spin frequency derivative ($\dot{\nu}$), and DMs but also consider Keplerian parameters describing the orbital motion. We employ Java script newfitorbit[21] to fit the Keplerian binary parameters: orbital period (P_b), the epoch of periastron passage (T_0), and projected semimajor axis (x). In this process, we assumed that both the longitude of periastron (ω) and the orbital eccentricity (e) are zero, resulting in a deviation from the initial ephemerides. For the binary system in near-circular orbit, it can be well described using the pulsar binary model ELL1 (C. Lange et al. 2001). In this model, the use of the time of ascending node ($T_{\rm asc}$) and Laplace−Lagrange parameters ($\epsilon_1 \equiv e \sin \omega$, $\epsilon_2 \equiv e \cos \omega$) in place of T_0, ω, and e is beneficial because employing $T_{\rm asc}$, ϵ_1, and ϵ_2 helps to break the high correlation between T_0 and ω in binary systems with low eccentricity. The substitution makes it easier to obtain phase-connected solutions. Then, according to the initial spin period and DM of the pulsar obtained, the pulses are folded with DSPSR[22] software (W. van Straten & M. Bailes 2011). Integrated profiles with 512 phase bins are obtained for each epoch. For the frequency channels and time subintegrations by affected strong narrowband and broadband radio frequency interference, these channels and subintegrations are zero-weighted with the PSRCHIVE[23] software package (A. W. Hotan et al. 2004). After aligning each observation and adding all observations, we employ the PSRCHIVE routine paas to generate a standard profile and employ PSRCHIVE's pat tool to create times of arrival (TOAs).

TEMPO (D. Nice et al. 2015) and TEMPO2 (G. B. Hobbs et al. 2006) were applied to build a phase-connected timing solution. We used the tool newfitorbit to obtain the initial timing solution of PSR J1602−0611, which is used as the initial ephemerides of the DRACULA[24] (P. C. C. Freire & A. Ridolfi 2018) iteration, ultimately resulting in the accurate timing solution for PSR J1602−0611. For the isolated pulsar, we fit the pulsar's positions, ν, $\dot{\nu}$. For the pulsar in binary systems, we fit the pulsar's positions, ν, $\dot{\nu}$, and five Keplerian orbital parameters (P_b, $T_{\rm asc}$, x, ϵ_1, ϵ_2).

We used the noise injection of each observation to calibrate the polarization and then select the observation with the highest signal-to-noise ratio of each pulsar to search for RM using the rmfit tool, including the contribution of Earth's ionosphere. For each pulsar, we search in the range of −10,000 to 10,000 rad m^{-2}, with a step size of 1. Furthermore, the DM was determined by dividing the entire frequency band into two subbands, each with a respective central frequency but the same bandwidth. The TOAs for these subbands were then fitted accordingly.

2.1. Flux Density

We calculated the flux density of pulsars according to the following radiometer equation (D. R. Lorimer & M. Kramer 2004):

$$S_{\rm mean} = \frac{\beta ({\rm S/N}) T_{\rm sys}}{G\sqrt{n_p t_{\rm obs} \Delta f}} \sqrt{\frac{\sigma}{1-\sigma}}, \quad (1)$$

where $S_{\rm mean}$ is the mean pulse flux density, in units of mJy; β is a correction factor for FAST, in our case, correlation factor $\beta = 1$; S/N stands for the signal-to-noise ratio of pulsars; $T_{\rm sys}$ is the system noise temperature (K); and G is the gain of the telescope (K Jy^{-1}). The system temperature is a function of the zenith angle $\theta_{\rm ZA}$, typically around 24 K, and is expressed as

$$T_{\rm sys} = P_0 \arctan(\sqrt{1+\theta_{\rm ZA}{}^n} - P_1) + P_2, \quad (2)$$

where the range of $\theta_{\rm ZA}$ is 0°−40°. The values of P_0, P_1, P_2, and n can be found in Table 4 of P. Jiang et al. (2020b). Parameter n_p is the polarization summed; observation duration is $t_{\rm obs}$, in units of seconds; Δf is observing bandwidth, in our case, an effective bandwidth of 400 MHz; and $\sigma = n_{\rm on}/n_{\rm bin}$ is the duty cycle. We applied Equation (2) to estimate the flux density of pulsars at 1250 MHz.

2.2. Rotating Vector Model

Pulsar polarization observations could lead to a well-defined PA, and we used the psrmodel tool of the PSRCHIVE software package to fit the RVM (V. Radhakrishnan & D. J. Cooke 1969). PA is described by the following formula:

$$\tan(\psi_0 - \psi) = \frac{\sin(\alpha)\sin(\phi_0 - \phi)}{\sin(\zeta)\cos(\alpha) - \cos(\zeta)\sin(\alpha)\cos(\phi_0 - \phi)}, \quad (3)$$

where ψ is the linear polarization PA, α is the magnetic inclination angle, ϕ is the pulsar rotational phase, $\zeta = \alpha + \beta$ (viewing angle), and ψ_0 and ϕ_0 represent the PA and rotational phase, respectively, associated with the fiducial plane.

3. Results

In this work, we report the timing solutions for nine isolated normal pulsars, two isolated MSPs, and one MSP in a binary system. The sample we selected consists of pulsars discovered by CRAFTS that, at the time of writing this paper, have an

[20] https://github.com/scottransom/presto
[21] https://github.com/SixByNine/newfitorbit
[22] http://dspsr.sourceforge.net/
[23] http://psrchive.sourceforge.net/
[24] https://github.com/pfreire163/Dracula

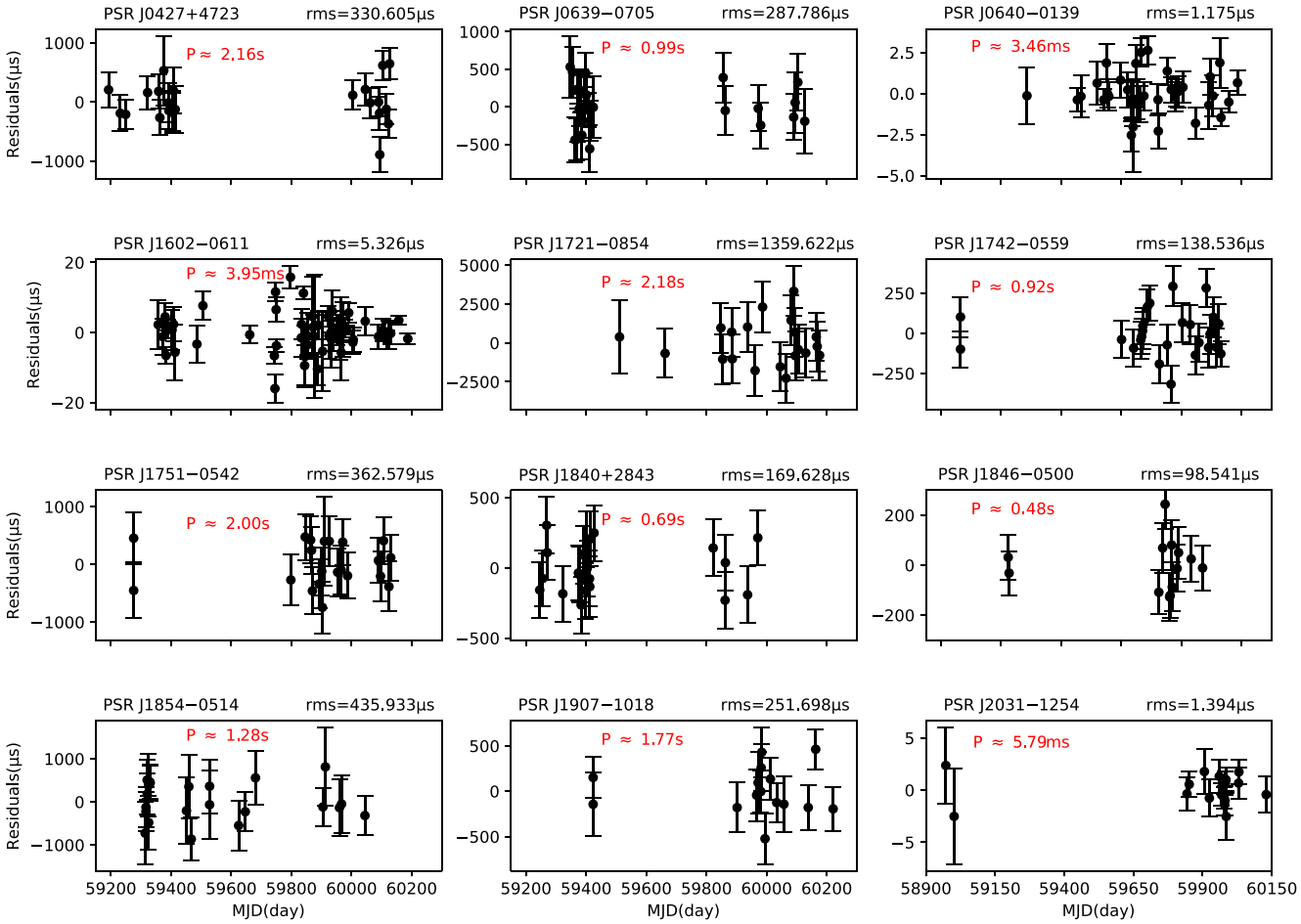

Figure 1. The best post-fit timing residuals of 12 pulsars. PSR J0640−0139 and PSR J2031−1254 are isolated MPSs, and PSR J1602−0611 is a binary system. In the figure, the MJD range shown is 58900−60300 for PSR J2031−1254, while the MJD range for the other pulsars is 59150−60300.

observational span of over 1 yr and do not yet have any timing solutions published. Other CRAFTS pulsars were excluded owing to either insufficient observational span or too few observations. The timing residuals are shown in Figure 1 with at least 1 yr of follow-up timing observations. It is worth noting that to ensure that the TOA residuals χ^2 are $\sim$1, we have scaled the TOA uncertainties by the so-called EFAC (EFAC is a parameter for scaling TOA errors and is used to correct instrument errors). These 12 pulsars timing solutions are reported in Tables 1–4, with JPL planetary ephemerides DE438,[25] in TCB units. We estimated the distance of the pulsar using the YMW16 model (J. M. Yao et al. 2017) and the NE2001 model (J. M. Cordes & T. J. W. Lazio 2002) for the Galactic distribution of free electrons. We determine the spin-down luminosity ($\dot{E} = 4\pi^2 I \dot{P} P^{-3}$), the surface magnetic field ($B_{\rm surf} = 3.2 \times 10^{19}(P\dot{P})^{1/2}$), and the characteristic age ($\tau_c = P/2\dot{P}$) from period and spin period derivative ($\dot{P}$).

We selected the observation with the highest S/N and drew a polarization figure, as shown in Figure 2. The black solid lines represent the integrated pulse profiles with linearly polarized emission (in red) and circularly polarized emission (in blue), respectively. According to the RM method described in Section 2, we calibrated the pulse profiles, and the results are presented in Table 5. We measured the pulse width at 10% and 50% of the profile peak, denoted as W_{10} and W_{50}, respectively.

[25] ftp://ssd.jpl.nasa.gov/pub/eph/planets/bsp/de438.bsp

Columns (5)–(7) in Table 5 give the fractional linear polarization L/S, the fractional net circular polarization V/S, and the fractional absolute circular polarization |V|/S. According to the radiometer Equation (2), the flux density of the pulsar at 1.25 GHz is calculated and presented in the last column of Table 5. The spin periods of the pulsars in this study range from 3.46 ms to 2.18 s, and their characteristic ages range from 1.43 Myr to 15.2 Gyr. We obtained the flux densities of these pulsars spanning from 16(6) to 492(60) μJy.

3.1. RVM Fitting

After calibration and RM fitting, only 3 of our 12 pulsars have sufficiently well-defined polarization position angle (PA) curves. Figure 3 shows the integrated polarization profile and viewing geometry obtained by fitting the RVM model.

PSR J1602−0611 is an MSP with a spin period of 3.95 ms and a DM of 27.626(1) cm^{-3} pc. From rmfit, we estimated the Faraday RM of PSR J1602−0611 to be 5(3) rad m^{-2}, with the measured linear and circular polarizations being 38.2(2)% and 2(2)%, respectively. Through the RVM fitting, we obtained the magnetic inclination angle, reference PA, fiducial plane longitude, and viewing angle with $\alpha = 84(16)^\circ$, $\psi_0 = 16(8)^\circ$, $\phi_0 = 192(4)^\circ$, and $\zeta = 74(16)^\circ$, respectively. The estimated DM distance is 1.4 and 1.9 kpc for the NE2001 model and YMW16 model, respectively.

PSR J1854−0514 is a pulsar with a spin period of 1.28 s and a DM of 281.1(2) cm^{-3} pc. From rmfit, it has a Faraday RM of

Table 1
Best-fitting Timing Parameters for PSR J0427−4723, PSR J0639−0704, PSR J0640−0139, and PSR J1721−0855

Parameter	PSR J0427+4723	PSR J0639−0704	PSR J0640−0139	PSR J1721−0855
Measured Parameters				
R.A., α (hh:mm:ss)	04:27:51.465(7)	06:39:58.644(10)	06:40:45.280643(8)	17:21:34.24(1)
decl., δ (dd:mm:ss)	+47:23:01.8(3)	−07:04:38.2(4)	−01:39:49.6639(3)	−08:55:08(1)
Pulse frequency, ν (s^{-1})	0.463298405496(4)	1.013699113957(3)	288.892720892735(1)	0.45843663480(2)
First derivative of pulse frequency, $\dot{\nu}$ (s^{-2})	$-5.1263(3) \times 10^{-15}$	$-1.67(3) \times 10^{-16}$	$-4.0879(5) \times 10^{-15}$	$-6.59(1) \times 10^{-16}$
Dispersion measure, DM (cm^{-3} pc)	54.0(2)	105.06(8)	149.983(2)	46.9(5)
Fitting Parameters				
First TOA (MJD)	59192.7	59347.3	59486.0	59662.9
Last TOA (MJD)	60127.0	60127.2	60186.1	60176.5
Timing epoch (MJD)	59598.0	59737.0	59680.0	59668.0
Data span (yr)	2.56	2.14	1.92	1.41
Number of TOAs	23	26	38	19
Solar system ephemerides model	DE438	DE438	DE438	DE438
rms timing residual (μs)	330.6	287.8	1.175	1359.6
TOA weighted factor, EFAC	1.1	1.1	1.4	4.9
Derived Parameters				
Galactic longitude, l (deg)	156.202	217.950	213.196	14.169
Galactic latitude, b (deg)	−1.017	−5.758	−3.135	15.385
DM distance, d (kpc)				
NE2001	1.4	4.0	5.7	1.6
YMW16	1.9	2.4	2.7	0.2
Characteristic age, τ_c (Myr)	1.43	96.34	1.12×10^{3}	11.01
Surface magnetic field, $B_{\rm surf}$ (10^{10} G)	7.27×10^{2}	40.50	4.17×10^{-2}	2.65×10^{2}
Spin-down luminosity, $\dot{E}$, (10^{30} erg s^{-1})	9.4	6.7	4.7×10^{4}	12

Table 2
Best-fitting Timing Parameters for PSR J1742−0559, PSR J1751−0542, PSR J1840+2843, and PSR J1846−0500

	PSR J1742−0559	PSR J1751−0542	PSR J1840+2843	PSR J1846−0500
Measured Parameters				
R.A., α (hh:mm:ss)	17:42:06.289(2)	17:51:32.606(7)	18:40:29.589(10)	18:46:26.917(8)
decl., δ (dd:mm:ss)	−05:59:57.79(11)	−05:42:16.2(3)	+28:43:13.7(3)	−05:00:19.5(9)
Pulse frequency, ν (s^{-1})	1.089112170924(3)	0.499654292364(4)	1.457509613559(6)	2.09803725694(3)
First derivative of pulse frequency, $\dot{\nu}$ (s^{-2})	$-7.408(2) \times 10^{-16}$	$-5.75(5) \times 10^{-17}$	$-2.2(5) \times 10^{-17}$	$-7.202(11) \times 10^{-15}$
Dispersion measure, DM (cm^{-3} pc)	98.23(9)	63.9(1)	63.7(1)	405.39(8)
Fitting Parameters				
First TOA (MJD)	59265.0	59276.0	59246.0	59423.6
Last TOA (MJD)	60130.6	60130.6	59971.1	60069.9
Timing epoch (MJD)	59618.0	59631.0	59608.0	59706.0
Data span (yr)	2.37	2.34	1.99	1.77
Number of TOAs	25	21	21	13
Solar system ephemerides model	DE438	DE438	DE438	DE438
rms timing residual (μs)	138.5	362.6	169.6	98.5
TOA weighted factor, EFAC	1.0	2.5	1.3	1.0
Derived Parameters				
Galactic longitude, l (deg)	19.420	20.854	57.938	27.909
Galactic latitude, b (deg)	12.477	10.573	14.855	−1.174
DM distance, d (kpc)				
NE2001	3.1	2.0	3.5	6.8
YMW16	1.0	0.6	6.2	6.5
Characteristic age, τ_c (Myr)	23.30	1.38×10^{2}	1.05×10^{3}	4.62
Surface magnetic field, $B_{\rm surf}$ (10^{10} G)	76.64	68.7	8.52	89.4
Spin-down luminosity, $\dot{E}$, (10^{30} erg s^{-1})	32	1.1	1.3	6.0×10^{2}

Table 3
Best-fitting Timing Parameters for PSR J1854−0514, PSR J1907−1018, and PSR J2031−1254

	PSR J1854−0514	PSR J1907−1018	PSR J2031−1254
Measured Parameters			
R.A., α (hh:mm:ss)	18:54:18.408(6)	19:07:42.088(6)	20:31:30.35440(4)
decl., δ (dd:mm:ss)	−05:14:26.1(5)	−10:18:42.5(4)	−12:54:28.826(3)
Pulse frequency, ν (s^{-1})	0.781281237119(6)	0.566323304509(2)	172.760569821455(4)
First derivative of pulse frequency, $\dot{\nu}$ (s^{-2})	$-1.1253(6) \times 10^{-15}$	$-2.3686(5) \times 10^{-15}$	$-1.796(6) \times 10^{-16}$
Dispersion measure, DM (cm^{-3} pc)	281.1(2)	90.99(8)	22.938(1)
Fitting Parameters			
First TOA (MJD)	59314.0	59423.6	58971.9
Last TOA (MJD)	60044.9	60221.5	60129.8
Timing epoch (MJD)	59640.0	59793.0	59478.0
Data span (yr)	2.00	2.18	3.17
Number of TOAs	22	15	17
Solar system ephemerides model	DE438	DE438	DE438
rms timing residual (μs)	435.9	251.7	1.394
TOA weighted factor, EFAC	3.0	4.8	1.4
Derived Parameters			
Galactic longitude, l (deg)	28.590	25.529	32.228
Galactic latitude, b (deg)	−3.023	−8.263	−27.951
DM distance, d (kpc)			
NE2001	6.1	2.7	1.1
YMW16	8.7	4.3	1.4
Characteristic age, τ_c (Myr)	11.0	3.79	1.52×10^4
Surface magnetic field, $B_{\rm surf}$ (10^{10} G)	1.55×10^2	3.65×10^2	1.89×10^{-2}
Spin-down luminosity, $\dot{E}$, (10^{30} erg s^{-1})	35	53	1.2×10^3

178(1) rad m^{-2}. Through the RVM method, we measured $\alpha = 74(8)°$, $\psi_0 = -18.1(4)°$, $\phi_0 = 178.6(3)°$, and $\zeta = 70(7)°$. The values obtained for the linear and circular polarization for this pulsar are 39(6)% and −8(2)%, respectively. The inferred pulsar distance is 6.1 and 8.7 kpc for the NE2001 model and YMW16 model, respectively. The spin-down luminosity and characteristic age of this pulsar are 3.5×10^{31} erg s^{-1} and 1.1×10^7 yr, respectively. PSR J1854−0514 exhibits a nulling phenomenon presented in Figure 4.

PSR J1907−1018 is a 1.77 s pulsar with DM of 90.99(8) cm^{-3} pc. We obtained a Faraday RM of 7(3) rad m^{-2} through rmfit; this estimated RM is the lowest in our source list. Through the RVM method, we found $\alpha = 88(2)°$, $\psi_0 = 61(7)°$, $\phi_0 = 179.8(1)°$, and $\zeta = 89(2)°$. The estimated linear polarization and circular polarization of this pulsar are 12(2)% and 11.20(3)%, respectively. The NE2001 model and YMW16 model predicted a DM distance of 2.7 and 4.3 kpc, respectively. This pulsar belongs to relatively young pulsars with a characteristic age of 3.79×10^6 yr and has a spin-down luminosity of 5.3×10^{31} erg s^{-1}. The single-pulse sequence displays pulse nulling phenomena for this pulsar (Figure 4).

3.2. Nulling

In our work, five pulsars display the phenomenon of pulse nulling; they are all normal pulsars, and their single-pulse sequences are shown in Figure 4. The pulse energy distributions for the on-pulse and off-pulse windows are shown in Figure 5. The on-pulse window was defined as the total longitude range over which significant pulsed emission is seen. The off-pulse energy was measured in an equal length of on-pulse bins. As can be seen from Figure 5, the on-pulse energy of each pulsar has a peak adjacent to zero. Following studies by R. T. Ritchings (1976), we calculate the nulling fraction (NF) by subtracting a scaled version of the off-pulse histogram from the on-pulse histogram until the sum of the difference counts in bins with $E < 0$ was zero. The uncertainty of NF is given by $\sqrt{n_p}/N$, where n_p is the number of null pulses and N is the total number of pulses (N. Wang et al. 2007). We choose observations with high signal-to-noise ratio to obtain the NF and then calculate the average value. The average NF values (expressed as NF_R) for the five pulsars are listed in the fifth column of Table 6.

Recent studies have found that R. T. Ritchings (1976) tends to overestimate the NF in its algorithm, especially for pulsars with weaker emission, leading to significant biases (D. L. Kaplan et al. 2018; A. Anumarlapudi et al. 2023). Here we employ a more robust mixture model method described by A. Anumarlapudi et al. (2023) to recalculate the NF (denoted as NF_A) for these five nulling pulsars, as shown in the last column of Table 6. Our calculations use the same data as previously used for calculating the NF. The results indicate that R. T. Ritchings (1976) may indeed overestimate the NF for some pulsars. However, it's worth noting that our effective exposure time per observation is only 4 minutes, which might introduce biases. This warrants further verification of their NF through longer observations in the future.

PSR J0639−0704 is a pulsar with a spin period of 0.98 s and a DM of 105.06 cm^{-3} pc. Through rmfit, we find an RM of 10(2) rad m^{-2} for this pulsar. The measured values of linear and circular polarization are 18(1)% and 1.1(2)%, respectively. With a DM of 105.06(8) cm^{-3} pc, the NE2001 model and YWM16 model predict a DM distance of 4.0 and 2.4 kpc, respectively. It has a low $\dot{E}$ of 6.7×10^{30} erg s^{-1} with a characteristic age of 9.63×10^7 yr. The pulse sequence of PSR 0639−0704 shows a nulling phenomenon (Figure 4). The single-pulse sequence of this pulsar indicates that it may exhibit

Table 4
Best-fitting Timing Parameters for PSR J1602−0611

Pulsar Name	PSR J1602−0611
Measured Parameters	
R.A., α (hh:mm:ss)	16:02:17.24172(5)
decl., δ (dd:mm:ss)	−06:11:43.475(2)
Pulse frequency, ν (s^{-1})	253.14146512594(1)
First derivative of pulse frequency, $\dot{\nu}$ (s^{-2})	$-3.03(1) \times 10^{-16}$
Dispersion measure, DM (cm^{-3} pc)	27.626(1)
Orbital period, P_b (days)	18.23999206(2)
Projected semimajor axis of orbit, x (lt-s)	12.179114(1)
TASC (MJD)	59805.5271999(3)
EPS1	$-1.94(2) \times 10^{-5}$
EPS2	$7.6(3) \times 10^{-6}$
Binary model	ELL1
Fitting Parameters	
First TOA (MJD)	59357.7
Last TOA (MJD)	60187.4
Timing epoch (MJD)	59805.5
Data span (yr)	2.27
Number of TOAs	55
Solar system ephemerides model	DE438
rms timing residual (μs)	5.3
TOA weighted factor, EFAC	3.7
Derived Parameters	
Galactic longitude, l (deg)	4.327
Galactic latitude, b (deg)	33.102
DM distance, d (kpc)	
NE2001	1.4
YMW16	1.9
Characteristic age, τ_c (Myr)	1.32×10^4
Surface magnetic field, $B_{\rm surf}$ (10^{10} G	1.38×10^{-2}
Spin-down luminosity, $\dot{E}$, (10^{30} erg s^{-1}	3.0×10^3
Inferred eccentricity, e (10^{-5})	2.08(2)
Mass function, f (10^{-3} $M_\odot$)	5.8(3)
Minimum companion mass, $m_{c,\rm min}$ ($M_\odot$)	0.2458
Median companion mass, $m_{c,\rm med}$ ($M_\odot$)	0.2889

the subpulse drifting phenomenon. Currently, due to the short duration of each observation, it is challenging to effectively analyze whether there is subpulse drifting behavior.

PSR J1721−0855 is a 2.18 s pulsar. The measured linear and circular polarizations of this pulsar are 34(2)% and −2(1)%, respectively, based on a Faraday RM of 10(3) rad m^{-2}. The distance based on the pulsar's DM of 46.9(5) cm^{-3} pc is 1.6 and 0.2 kpc for the NE2001 model and YMW16 model, respectively. The estimated DM distance is the nearest for this pulsar in our source list. With a characteristic age of 1.1×10^7 yr, PSR J1721−0855 is an old pulsar having $\dot{E}$ of 1.2×10^{31} erg s^{-1}, and this pulsar shows a nulling phenomenon, presented in Figure 4.

From Figure 4, we observe that PSR J1854−0514 not only exhibits pulsar nulling phenomena but also demonstrates mode-changing characteristics. This is a double-peaked profile pulsar. To differentiate between the two distinct modes of this pulsar, we define the minimum intensity between two adjacent components as the boundary separating the double-peaked profile. When the peak pulse intensity on the left exceeds that on the right, we define it as Mode A. Conversely, it is defined as Mode B. We have stacked a total of 36 minutes of observations of this pulsar and present the mean pulse profiles of its two distinct modes in Figure 6. Mode A and Mode B account for approximately 25% and 75% of the total data, respectively.

3.3. Subpulse Drifting

PSR J1840+2843 shows an apparently periodic subpulse drifting phenomenon. We plotted the two-dimensional fluctuation spectrum (2DFS; R. T. Edwards & B. W. Stappers 2002) in Figure 7. The frequency axis of 2DFS corresponds to P/P_3, where P is the pulsar rotation period and P_3 represents the periodicity of subpulse drifting. The horizontal frequency axis of 2DFS corresponds to P/P_2, where P_2 represents the characteristic horizontal time separation between drifting bands.

In Figure 7, the side panel of the 2DFS shows a clear spectral peak occurring between 0.1246 and 0.1254 cycles per period. This spectral feature corresponds to the characteristic $P_3 = 7.99 \pm 0.02P$. There are two peaks in the bottom panel of 2DFS, with the peak on the right corresponding to the horizontal drifting period of drift bands. This spectral feature corresponds to the characteristic $P_2 = 9^\circ.25 \pm 0.^\circ04$.

3.4. The Traditional Death Line

Figure 8 displays 69 newly discovered pulsars from CRAFTS on a $P-\dot{P}$ diagram, compared with the known pulsars listed in PSRCAT (ver. 1.70). These 69 new pulsars consist of 11 pulsars reported in A. D. Cameron et al. (2020), 10 pulsars reported in M. Cruces et al. (2021), 12 MSPs reported in C. C. Miao et al. (2023), 24 pulsars reported in Q. D. Wu et al. (2023a), and 12 pulsars reported in this work.

According to D. Bhattacharya et al. (1992), the expression for the traditional death line is

$$(B_s/10^{12})/P^2 = 0.17, \quad (4)$$

which corresponds to a spin-down luminosity ($\dot{E}$) of 1.53×10^{30} erg s^{-1}. When the spin-down luminosity is lower than 1.53×10^{30} erg s^{-1}, the pulsar exceeds the traditional death line in the $P - \dot{P}$ diagram. In this work, two pulsars (PSR J1751−0542 and PSR J1840+2843) are located below the traditional death line in the $P - \dot{P}$ diagram.

PSR J1751−0542 is a 2.00 s pulsar with a DM of 63.9(1) cm^{-3} pc. This pulsar has a Faraday RM of 73(1) rad m^{-2}; the linear and circular polarizations of this pulsar are 27(3)% and 1.5(5)%, respectively. PSR J1751−0542 has a spin-down luminosity of 1.1×10^{30} erg s^{-1} and a characteristic age of 1.38×10^8 yr. Only 40 pulsars have $\dot{E}$ lower than this pulsar. The single-pulse sequence of this pulsar shows a nulling phenomenon (Figure 4). The NE2001 model predicted a DM distance of 2.0 kpc, while the YMW16 model predicted a DM distance of 0.6 kpc.

PSR J1840+2843 has a period of 0.69 s, a characteristic age of 1.05×10^9 yr, and a spin-down luminosity of 1.3×10^{30} erg s^{-1}, below the traditional death line. Only 46 pulsars have $\dot{E}$ lower than this pulsar. This pulsar shows a subpulse drifting phenomenon as shown in Figure 4. It has a DM of 63.7(1) cm^{-3} pc and a Faraday RM of 75(1) rad m^{-2}. The linear and circular polarizations are 22(1)% and 5.3(5)%, respectively. The estimated pulsar distance is 3.5 and 6.2 kpc for the NE2001 model and YMW16 model, respectively.

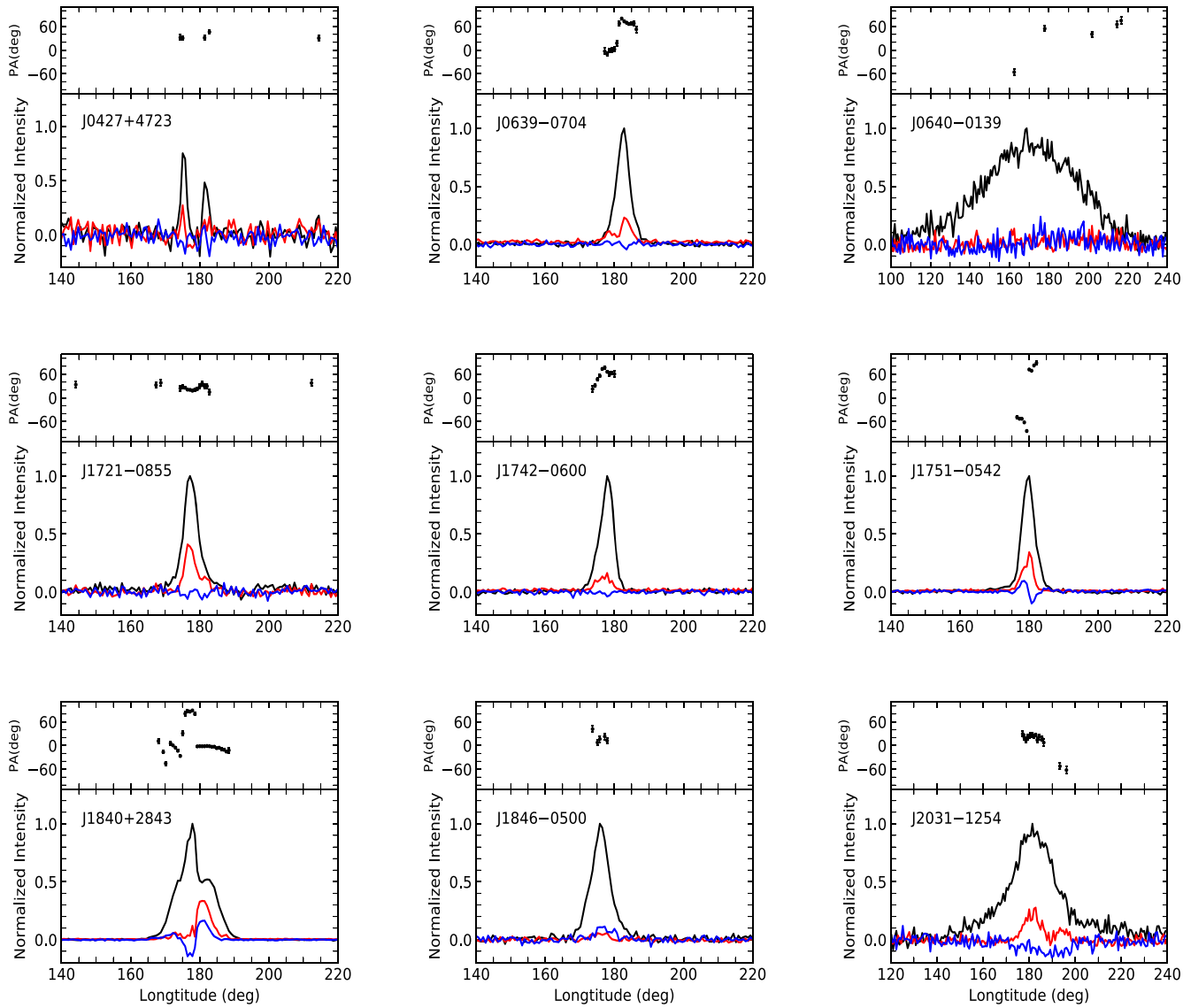

Figure 2. Integrated pulse profiles for nine pulsars, PSR J0427+4723, PSR J0639−0704, PSR J0640−0139, PSR J1721−0855, PSR J1742−0600, PSR J1751−0542, PSR J1840+2843, PSR J1846−0500, and PSR J2031−1254. The black line in the lower panel of each subplot represents the total intensity, and the red line and blue line represent the linear polarization intensity and circular polarization intensity, respectively. From the plot, it can be seen that the peak intensity is normalized to 1.

Table 5
Pulse Width at 50% and 10% of the Profile Peak, Rotation Measure, Polarization Parameters (L/S, V/S, and |V|/S), and Flux Density

Pulsar	P (s)	W_{10} (ms)	W_{50} (ms)	RM (rad m^{-2})	L/S (%)	V/S (%)	|V|/S (%)	$S_{1.25\ \mathrm{GHz}}$ (μJy)
PSR J0427+4723	2.16	26.4(3)	22.0(3)	431(21)	12.5(2)	−25(8)	37(8)	16(6)
PSR J0639−0704	0.99	28.5(3)	12.7(3)	10(2)	18(1)	1.1(2)	4.6(2)	100(4)
PSR J0640−0139	3.46×10^{-3}	3.31(4)	1.60(4)	168(16)	3(1)	2.2(3)	12.5(3)	189(14)
PSR J1602−0611	3.95×10^{-3}	2.68(5)	1.48(5)	5(3)	38.2(2)	2(2)	8(2)	97(3)
PSR J1721−0855	2.18	28.5(8)	12.7(8)	10(3)	34(2)	−2(1)	6(1)	216(19)
PSR J1742−0559	0.92	25.1(1)	11.6(1)	75(1)	16(4)	−1.5(9)	2.6(9)	222(19)
PSR J1751−0542	2.00	24.6(4)	11.9(4)	73(1)	27(3)	1.5(5)	9.1(5)	258(31)
PSR J1840+2843	0.69	52.8(1)	28.5(1)	75(1)	22(1)	5.3(5)	13.8(5)	492(60)
PSR J1846−0500	0.48	33.4(1)	15.1(1)	381(18)	4.4(6)	10.1(2)	10.3(3)	99(7)
PSR J1854−0514	1.28	33.5(5)	10.5(5)	178(1)	39(6)	−8(2)	10(2)	90(10)
PSR J1907−1018	1.77	14.9(1)	6.9(1)	7(3)	12(2)	11.20(3)	11.20(3)	95(19)
PSR J2031−1254	5.79×10^{-3}	2.10(2)	0.56(2)	−7(4)	13.1(8)	−12.8(2)	12.8(2)	132(12)

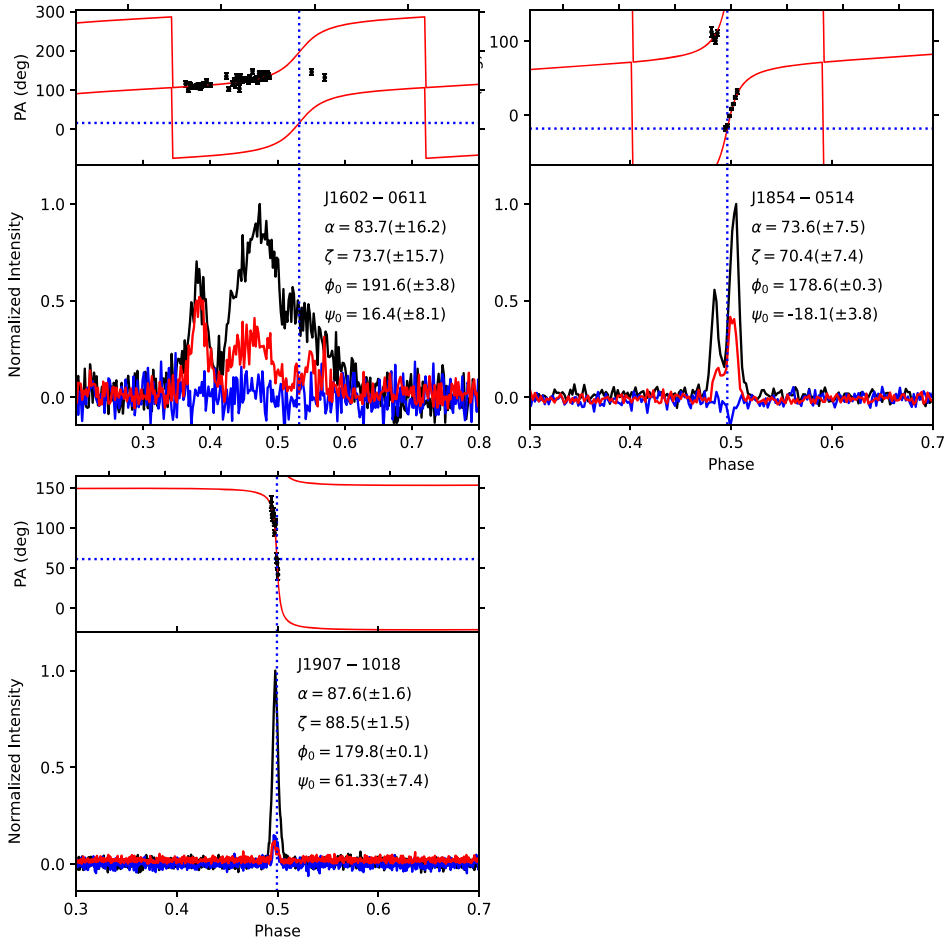

Figure 3. Integrated polarization profiles and viewing geometry of PSR J1602−0611, PSR J1854−0514, and PSR J1907−1018. The points in the upper panel of each subplot are the polarization PAs, and the errors are given. The red line on the upper panel represents the best fit result of the RVM model. Polarization PA of four pulsars is >4 times the PA errors.

3.5. Millisecond Pulsars

In this work, a total of three MSPs are reported, two of which are isolated MSPs (PSR J0640−0139 and PSR J2031−1254) and one of which is in a binary system (PSR J1602−0611).

The rotation period of PSR J0640−0139 is 3.46 ms, with a stable spin-down rate of $4.8981(6) \times 10^{-20}$ s s^{-1}. From rmfit, it has a Faraday RM of 168(16) rad m^{-2}. The linear and circular polarizations for PSR J0640−0139 were measured to be low with 3(1)% and 2.2(3)%, respectively. With a DM of 149.983(2) cm^{-3} pc, the NE2001 model and YWM16 model predict a distance of 5.7 and 2.7 kpc, respectively. It is an energetic pulsar that has a spin-down luminosity of 4.7×10^{34} erg s^{-1}, which exceeds the energy loss rate threshold of 3×10^{34} erg s^{-1} for a potential gamma-ray pulsar (D. J. Thompson et al. 1999). We checked the observation source[26] of the Fermi Gamma-ray Space Telescope, but no gamma-ray counterpart is found for this pulsar.

PSR J1602−0611 is an MSP with a spin period of 3.95 ms and a DM of 27.626(1) cm^{-3} pc. It is in an 18.24-day binary orbit with an eccentricity of 2.03×10^{-5}. This pulsar has not detected signals in many observations (red circles in Figure 9). We used Equation (2) to calculate the flux density of all visible signals of PSR J1602−0611 (Figure 10), and it can be seen that the flux density of PSR J1602−0611 varies immensely, with the ratio of the highest value to the lowest one being 35.2. Among them, the one with the lowest flux density is 11.96 μJy. It is close to the flux density limit of FAST observation for 4 minutes (∼5.34 μJy; red solid line in Figure 10). Therefore, we suspect that the non-detection may be attributed to interstellar scintillation or variations in the pulsar's flux density due to changes in the particle flow from the pulsar's magnetosphere. We used the corresponding Python script in package dynsp_acf[27] to estimate the scintillation timescale of the source, which is 2.35(2) minutes. As the exposure time is short, with 4 minutes each epoch, the causes of non-detection and flux variations need further investigations. To investigate whether there is an eclipse in PSR J1602−0611, we show in Figure 9 the timing residuals plotted against the orbital phase. No noticeable trend is seen. This pulsar has a wide pulse profile. The pulse widths W_{10} and W_{50} are 2.6841 and 1.4834 ms, respectively. Assuming that the mass of the pulsar is 1.4 $M_\odot$, the mass function of the system is 0.0058(3) $M_\odot$ and the minimum mass of the companion star is 0.2458 $M_\odot$. According to the orbital parameters of this pulsar and the minimum mass of the companion star, the companion is most likely a He WD.

[26] https://heasarc.gsfc.nasa.gov/cgi-bin/W3Browse/

[27] https://github.com/larskuenkel/dynsp_acf

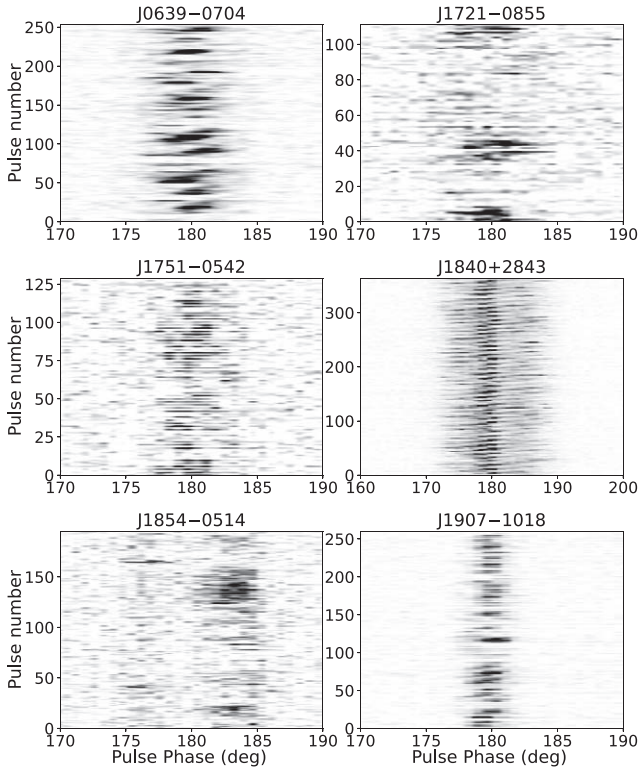

Figure 4. Single-pulse sequences display pulse nulling phenomena for five newly discovered pulsars, PSR J0639−0704, PSR J1721−0855, PSR J1751−0542, PSR J1854−0514, and PSR J1907−1018. PSR J1840+2843 shows the subpulse drift phenomenon.

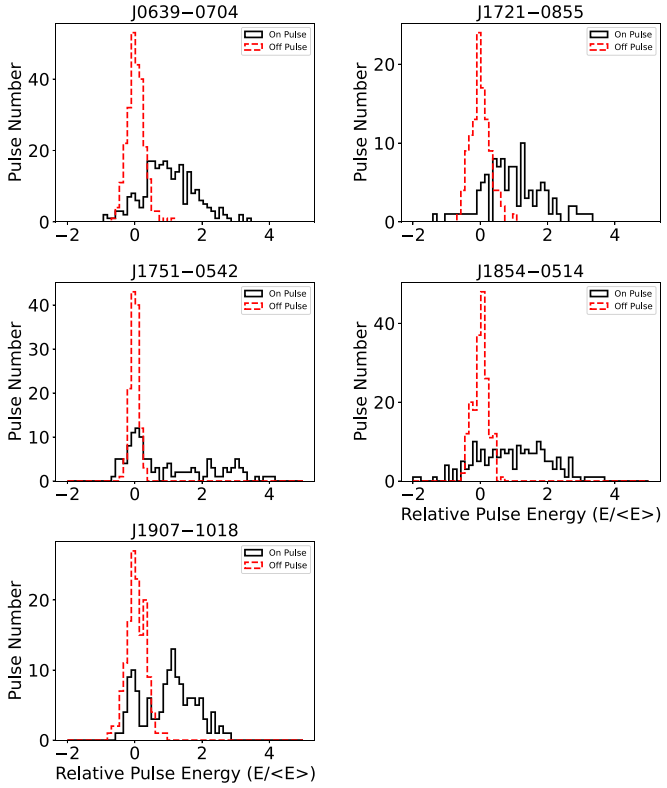

Figure 5. Pulse energy distributions for the on-pulse (black solid histogram) and off-pulse (red dashed histogram) regions for five pulsars. The energies are normalized by the mean on-pulse energy.

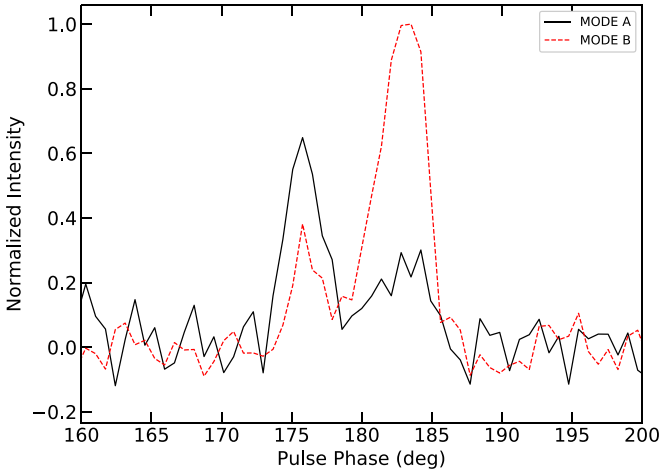

Figure 6. The mean pulse profiles of the two distinct modes of PSR J1854−0514.

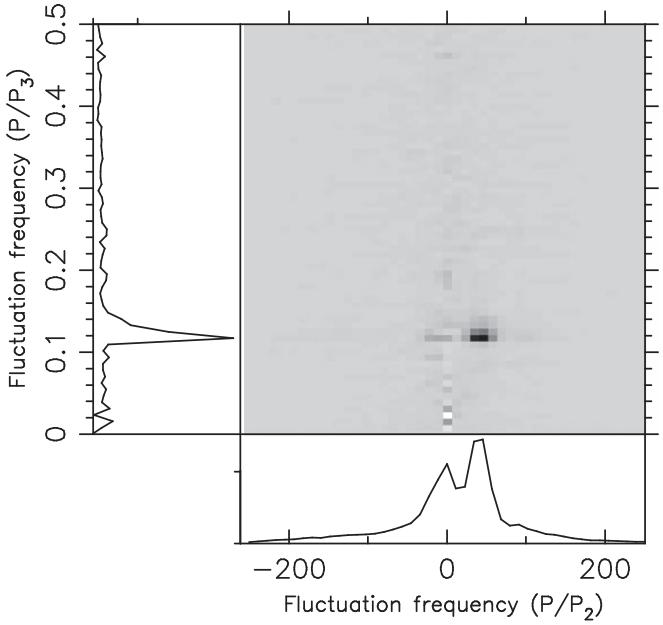

Figure 7. The 2DFS for the PSR J1840+2843. The left panel shows significant peaks between 0.1246 and 0.1254 cycles per period, indicating that the pulsar exhibits strong periodic intensity variations. The bottom panel is asymmetric at the 0 axis, suggesting the presence of drifting phenomena in this pulsar.

Table 6
The Average Nulling Fractions for Five Pulsars

Pulsar	T_{obs} (minutes)	N_{tot}	N_{null}	NF_R (%)	NF_A (%)
PSR J0639−0704	52.8	3220	1196	37(4)	8(1)
PSR J1721−0855	36.6	1012	335	31(5)	14(4)
PSR J1751−0542	37.2	1123	444	45(6)	24(3)
PSR J1854−0514	36.0	1692	546	33(4)	4(2)
PSR J1907−1018	44.6	1524	489	30(5)	16(2)

Note. T_{obs}, N_{tot}, and N_{null} represent the duration, the total number of pulses, and the number of null pulses of observations, respectively. The NF_R and NF_A represent the NF calculated using the methods of R. T. Ritchings (1976) and A. Anumarlapudi et al. (2023), respectively.

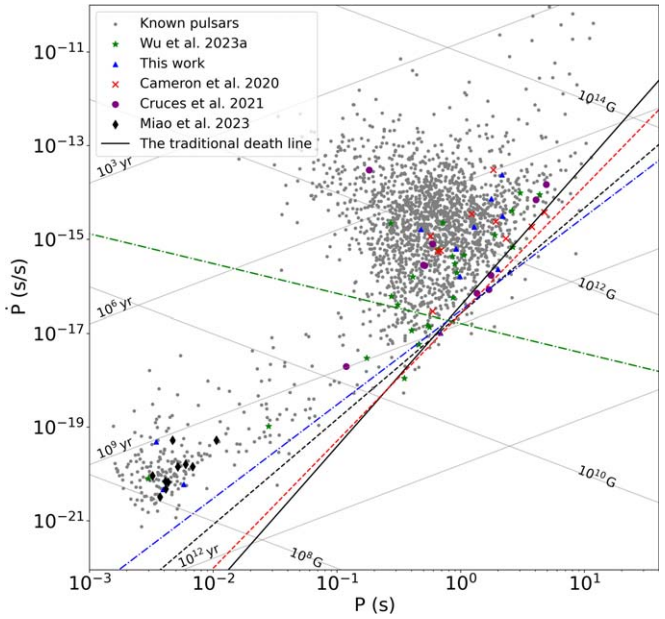

Figure 8. A $P - \dot{P}$ diagram of known pulsars and new pulsars presented in this work. The gray circles are known pulsars. The green stars represent pulsars reported in Q. D. Wu et al. (2023a). The red crosses represent pulsars reported in A. D. Cameron et al. (2020). The purple circles represent pulsars reported in M. Cruces et al. (2021). The black diamonds represent pulsars reported in C. C. Miao et al. (2023). The blue triangles represent pulsars reported in this work. We used several colored lines to plot the death line under different death line models; pulsars below the death lines are not expected to emit radio signals. The traditional death line (D. Bhattacharya et al. 1992) is the black line. Formula (9) in K. Chen & M. Ruderman (1993) corresponds to a red dashed death line. The black dashed line and blue dashed line are based on curvature radiation from the vacuum gap model and the SCLF model as proposed by B. Zhang et al. (2000). The green dashed line is based on SCLF models for inverse Compton scattering.

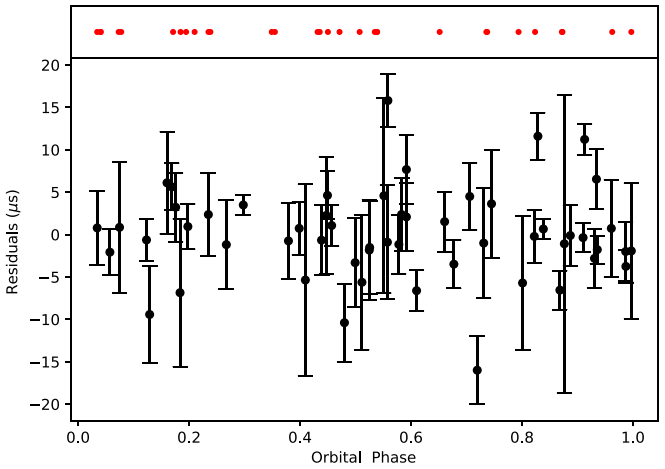

Figure 9. Timing residuals with binary orbit phase for PSR J1602−0611, based on the timing solution presented in Table 4. The red circles represent observations without pulse signals. In order to see them more clearly, we have placed them in the upper subplot.

PSR J2031−1254 is an isolated MSP with a spin period of 5.79 ms and a DM of 22.938(1) cm^{-3} pc. This pulsar has a stable spin-down rate of $6.02(2) \times 10^{-21}$ s s^{-1} and Faraday RM of −7(4) rad m^{-2}. The estimated linear and circular polarizations of this pulsar are 13.1(8)% and −12.8(2)%, respectively. The distance inferred based on the pulsar's DM of 22.938(1) cm^{-3} pc is 1.1 and 1.4 kpc for the NE2001 model and YMW16 model, respectively. This pulsar has a spin-down luminosity of 1.2×10^{33} erg s^{-1}.

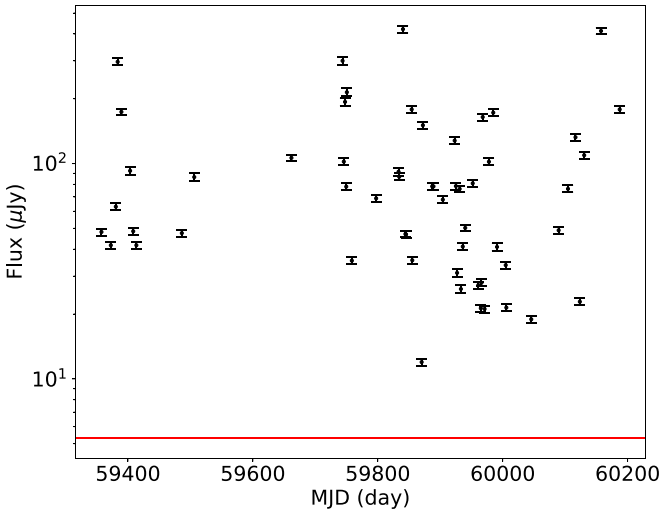

Figure 10. Flux density of PSR J1602−0611. The red solid line represents the flux density limit for FAST observation for 4 minutes.

3.6. The Remaining Pulsars

PSR J0427+4723 is a sharp double-peaked pulsar with a spin period of 2.15 s. The left component of the pulse profile is dominant. This pulsar has a high Faraday RM of 431(21) rad m^{-2}, and the linear and circular polarizations for PSR J0427+4723 were measured to be 12.5(2)% and −25 (8)%, respectively. With a DM of 54.0(2) cm^{-3} pc, the NE2001 model and YWM16 model predict DM distances of 1.4 and 1.9 kpc, respectively. The characteristic age of this pulsar is 1.43 $\times 10^6$ yr, indicating that it is a relatively young pulsar.

PSR J1742−0559 has a period of 0.92 s. We find an RM of 75(1) rad m^{-2} through rmfit for this pulsar, and the measured values of the linear and circular polarization are 16(4)% and −1.5(9)%, respectively. With a DM of 98.23(9) cm^{-3} pc, the obtained pulsar's distance is 3.1 and 1.0 kpc for the NE2001 model and YMW16 model, respectively. The spin-down luminosity and characteristic age of this pulsar are 3.2×10^{31} erg s^{-1} and 2.33×10^7 yr, respectively.

PSR J1846−0500 is a pulsar with a period of 0.48 s. This pulsar has a higher Faraday RM of 381(18) rad m^{-2}. The obtained linear and circular polarizations of this pulsar are 4.4 (6)% and 10.1(2)%, respectively. This pulsar has the highest DM of 405.39(8) cm^{-3} pc in our sample. The NE2001 model and YMW16 model predicted DM distances of 6.8 and 6.5 kpc, respectively. This pulsar has a spin-down luminosity of 6.0×10^{32} erg s^{-1} and belongs to relatively young pulsars with a characteristic age of 4.62×10^6 yr.

4. Discussion

We reported the timing results of 12 new pulsars from CRAFTS. These pulsars have spin periods ranging from 3.46 ms to 2.18 s, and their characteristic ages range from 1.43 Myr to 15.2 Gyr. We obtained the flux densities of these pulsars spanning from 16(6) to 492(60) μJy. None of the 12 pulsars are associated with Galactic supernova remnants[28] (D. A. Green 2019). We reported these new pulsars' phase-

[28] http://www.mrao.cam.ac.uk/surveys/snrs/

Table 7
The Average Values of P and $\dot{P}$ for Pulsars below the Traditional Death Line (A) and Normal Pulsars (B)

	P (s)	$\dot{P}$ (s s^{-1})
A	3.125	2.630×10^{-15}
B	0.887	4.823×10^{-13}

Note. The definition of normal pulsars is pulsars with a spin period greater than 30 ms.

connected timing ephemerides, polarization profiles, and Faraday RMs. Nine out of the 12 pulsars are normal pulsars; the other three are MSPs. Among these pulsars, five show the phenomenon of pulse nulling, and one pulsar shows subpulse drift phenomena (Figure 4). In our work, PSR J0640−0139 and PSR J2031−1254 are isolated MSPs.

4.1. Testing Radiation Theory

Out of the 3400 pulsars in the pulsar population, there are 62 below the death line, which corresponds to ∼1.9% of the entire population. The periods of these 62 pulsars span from 0.3456 to 75.89 s, with period derivatives between 0.00054×10^{-18} s s^{-1} and 255×10^{-15} s s^{-1} and ages between 3.24×10^{6} yr and 10.1×10^{9} yr.

A series of Parkes surveys using multibeam receivers have discovered ∼1261 pulsars so far, of which only 27 pulsars are below the death line (data are from ATNF ver. 1.70), indicating a 2.2% occurrence. At present, of the 72 CRAFTS pulsars with spin-down rate reported, 10 (including two from this work) are located below the traditional death line, implying a ratio of 14%. These comparisons suggest that FAST can find more pulsars below the traditional death line, which means that FAST has higher sensitivity.

We calculated the average values of P and $\dot{P}$ for pulsars below the traditional death line and normal pulsars (Table 7). It can be seen that the average $\dot{P}$ of pulsars below the traditional death line is two orders of magnitude smaller than the average $\dot{P}$ of normal pulsars. Additionally, their periods are relatively large, indicating that pulsars below the traditional death line have older ages.

PSR J1751−0542 exhibits a pulse nulling phenomenon, and PSR J1840+2843 shows a subpulse drift phenomenon. Furthermore, it should be noted that not all pulsars below the death line are nulling pulsars.

Figure 8 shows death lines for various models. Each death line corresponds to a point where the radio emission from a pulsar is expected to be turned off owing to insufficient electron pairs. The black solid line represents the traditional death line model, where inadequate potential in the polar cap leads to the pulsar being radio-quiet (M. A. Ruderman & P. G. Sutherland 1975; D. Bhattacharya et al. 1992). The red dashed line, referred to as the K. Chen & M. Ruderman (1993) model, considers complex magnetic structures with highly curved field lines. The black dashed line and blue dashed line correspond to the vacuum gap model and the SCLF model, respectively (B. Zhang et al. 2000). These models were obtained by considering curvature radiation and inverse Compton scattering under the general relativistic frame-dragging effect (J. Arons & E. T. Scharlemann 1979).

PSR J0901−4046 has a spin period of 75.88 s, making it the longest known pulsar in terms of spin period (M. Caleb et al. 2022). It is located above the death line of the SCLF radio emission model. This indicates that in the presence of a multipolar magnetic field configuration, nonrelativistic charges can flow from the polar cap. PSR J1751−0542 can also be explained using this model, but PSR J1840+2843 is located below this model. It is hoped that in the future more low-$\dot{E}$ pulsars can be found to test radiation theory.

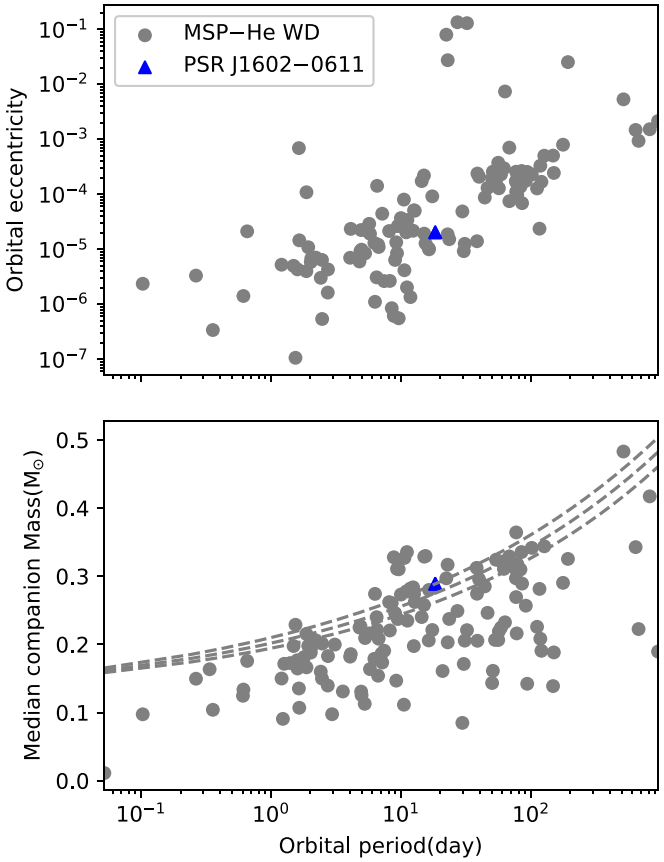

Figure 11. The MSPs with with light WD companions from PSRCAT (ver. 1.70). MSP−He WD systems are shown with gray circles. Top panel: the correlation between orbital period and eccentricity of MSP and light WD companion systems. Bottom panel: the correlation between orbital period and companion mass of MSP and light WD companion systems. The dashed lines are the numerical calculations of the MSP−He WD system by T. M. Tauris & G. J. Savonije (1999). The median companion mass estimation is given based on their mass functions assuming an orbital inclination of $i = 60°$ and $M_{\rm psr} = 1.4\,M_{\odot}$.

4.2. The Possible MSP−He WD Binary System

MSPs are spun up through accreting matter and angular momentum from companion stars (D. Bhattacharya & E. P. J. van den Heuvel 1991). During the transition to MSP, the magnetic field strength will decrease (usually from 10^{12} to 10^{8} G) owing to aging (P. Goldreich & A. Reisenegger 1992) or accretion (G. S. Bisnovatyi-Kogan & B. V. Komberg 1974). The surface magnetic field strength of PSR J1602−0611 is 1.38×10^{8} G. Assuming that the mass of the pulsar is $1.4\,M_{\odot}$ and the orbital inclination i is 60°, according to the mass function, the median companion mass of PSR J1602−0611 is $0.2889\,M_{\odot}$. T. M. Tauris & G. J. Savonije (1999) proposed a companion mass prediction for MSP and He WD systems (Figure 11, bottom panel). T. M. Tauris & G. J. Savonije (1999) predicted the correlation between orbital and companion mass for MSP−He WD systems, as depicted in the bottom panel of Figure 11 with black dashed lines. We found that the

orbital period and the companion mass distribution of PSR J1602−0611 are consistent with MSP−He WD systems. The distribution of orbital period and eccentricity of PSR J1602−0611 also conforms to MSP−He WD systems (Figure 11, top panel). Therefore, we believe that this pulsar belongs to the MSP−He WD systems. MSP−He WD systems in globular clusters are not considered in our sample because the complex situation in globular clusters may make the eccentricity of the other stars in this system inaccurate.

4.3. Nulling Phenomenon

Although recent results suggest that the method proposed by R. T. Ritchings (1976) may overestimate the NF values, this needs to be validated with larger samples in the future. Since most prior research has used the R. T. Ritchings (1976) method to estimate the NF, for consistency we still use the NF obtained from the R. T. Ritchings (1976) method in this study to compare with the NF of known nulling pulsars and provide a brief discussion.

From the normalized single-pulse energy distribution, we calculated the NF for these pulsars, with the largest one being around 45%. In Figure 12, we plot the $P - \dot{P}$ diagram of the nulling pulsars newly discovered by FAST. It seems that the new nulling pulsars discovered by FAST are often long-period or old pulsars, which are near or even exceed the traditional death line. This means that they all have relatively lower $\dot{E}$. From Figures 8 and 12, we can see that not all of the old or long-period pulsars found by FAST have pulse nulling phenomena. This suggests that not all pulsars near or even beyond the traditional death line will exhibit the nulling behavior and that FAST's high sensitivity enables the detection of more low-$\dot{E}$ pulsars and facilitates testing of the radiation theory.

In order to compare the distribution of nulling pulsars in our work with known nulling pulsars, we plotted the relationship between NF and period, τ_c, $\dot{P}$, and $\dot{E}$ of nulling pulsars in Figure 13. It can be seen that the nulling pulsars in our work have a larger period and larger NF as shown in panel (a). And panel (b) shows that the nulling pulsars in our work are older. The distribution of $\dot{P}$ is relatively uniform (panel (c)). Moreover, it can be seen that the nulling pulsars we found have lower $\dot{E}$, and one nulling pulsar in our work has the lowest $\dot{E}$ among these known nulling pulsars. Often, pulsars with older age have larger NFs, while pulsars with larger $\dot{E}$ tend to have smaller NFs. The relationship between long periods and large NF is the most significant (J. D. Biggs 1992; P. F. Wang et al. 2020), and the nulling pulsars in our study also confirm these relationships.

4.4. Flux Density and Luminosity

It is difficult to determine the luminosity of a pulsar, but we can calculate the monochromatic luminosity (D. R. Lorimer & M. Kramer 2012; A. Szary et al. 2014) based on the formula

$$L_v \equiv S_v d^2, \tag{5}$$

where S_v is the mean flux density measured at different frequencies.

In order to compare its average flux density with that of known pulsars, their flux densities at 1400 MHz are calculated using a pulsar spectral index. In this study, we utilize the

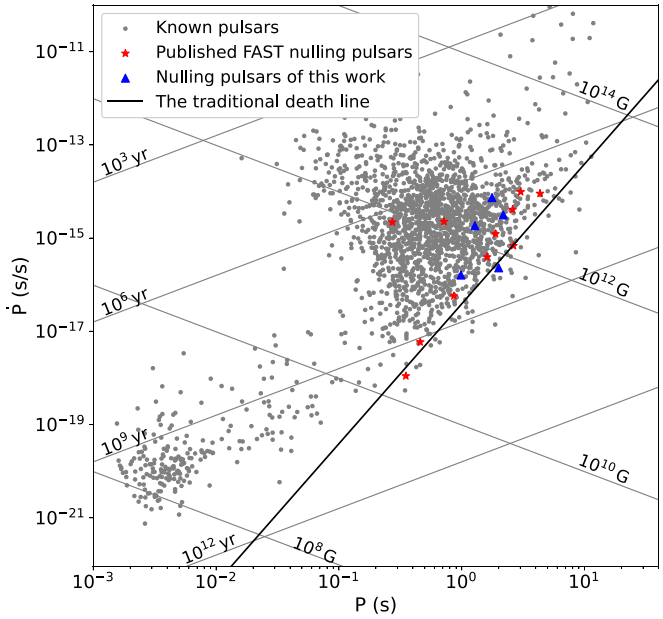

Figure 12. A $P - \dot{P}$ diagram of known pulsars and FAST's newly discovered nulling pulsars. The gray circles are known pulsars. The red stars represent the published nulling pulsars discovered by FAST. The nulling pulsars in our study are represented by the blue triangles.

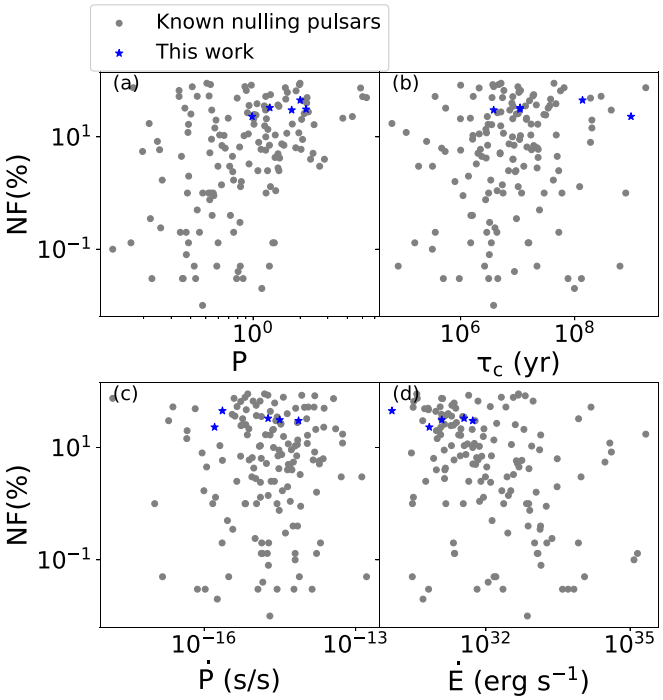

Figure 13. The correlations between NF and pulsar period, τ_c, $\dot{P}$, and $\dot{E}$. The gray circles in the figure come from P. F. Wang et al. (2020).

average spectral index of −1.64 from H. W. Xu et al. (2024) to calculate the flux density of pulsars at 1400 MHz.

As shown in panel (a) of Figure 14, we present the pulsar $\dot{E}$ and flux (S_{1400}) distribution reported for 35 CRAFTS pulsars. The flux density of 35 pulsars discovered with FAST is significantly lower than that of most known pulsars. From panel (b) of Figure 14, we can see that the new pulsars discovered by FAST have a low flux density within a similar range. This also indicates that FAST has a very high sensitivity

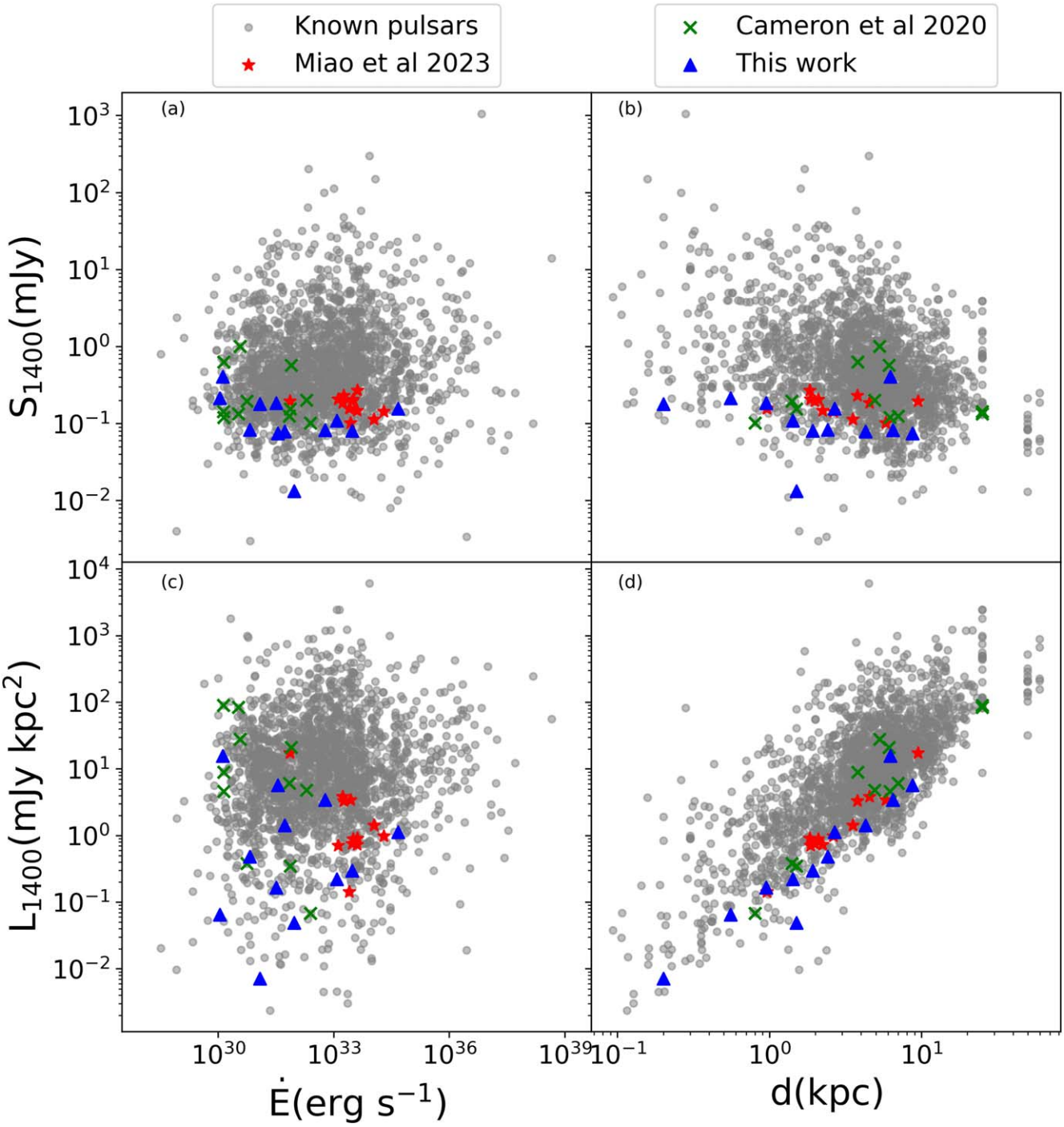

Figure 14. Panels (a) and (c) show the distributions of the mean flux density and the radio luminosity (L_{1400}) on spin-down luminosity ($\dot{E}$), respectively. Panels (b) and (d) show the dependence of the mean flux density and the radio luminosity on the distance from YMW16, respectively. The blue triangles represent pulsars reported in this work. The green crosses stand for CRAFTS pulsars in A. D. Cameron et al. (2020), and red stars are CRAFTS MSPs in C. C. Miao et al. (2023). Other known pulsars are represented by gray circles, and the data are from ATNF (ver. 1.70).

and is very effective for detecting weak sources. Panel (c) of Figure 14 shows the dependence of radio luminosity on $\dot{E}$ for 35 pulsars and other known pulsars. Previous research has shown that the correlation between radio luminosity and $\dot{E}$ is very weak (D. R. Lorimer et al. 1993; I. F. Malov & O. I. Malov 2006; A. Szary et al. 2014; Q.-D. Wu et al. 2020). From panel (c), it can be observed that these weak sources did not change the weak correlation between L and $\dot{E}$. Panel (d) of Figure 14 shows the distance distribution of FAST pulsars versus luminosity. We found that in the same luminosity range the pulsars discovered by FAST are farther away from us; at the same distance, the pulsars found by FAST have lower luminosity. In Figure 15, we present the spin-down luminosity ($\dot{E}$) versus characteristic age (τ_c) distribution of 69 pulsars newly discovered by FAST. It shows that the pulsars newly discovered by FAST are older and $\dot{E}$ is lower than in the known pulsars. The pulsar in our work has a lower $\dot{E}$ at the same characteristic age. FAST's enhanced sensitivity not only

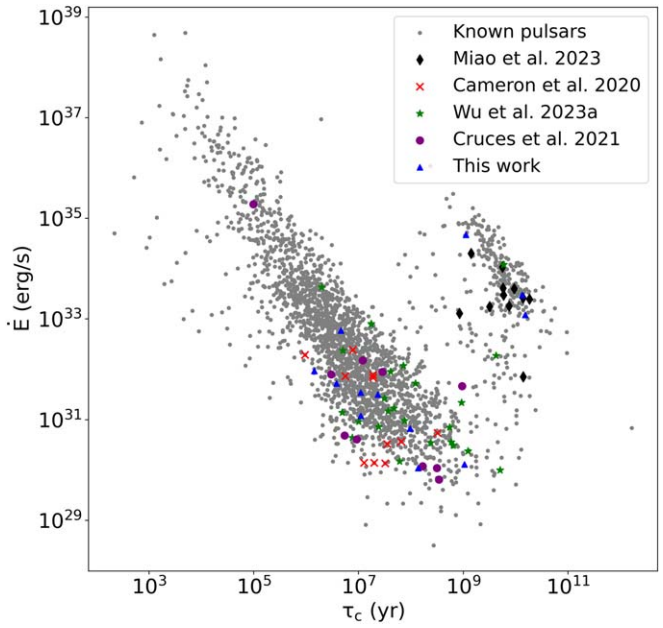

Figure 15. The distribution of the spin-down luminosity($\dot{E}$) over characteristic age (τ_c). The green stars represent pulsars reported in Q. D. Wu et al. (2023a). The red crosses stand for CRAFTS pulsars in A. D. Cameron et al. (2020). The purple circles represent pulsars reported in M. Cruces et al. (2021). The black diamonds stand for CRAFTS MSPs in C. C. Miao et al. (2023). The blue triangles represent pulsars reported in this work. Other known pulsars are represented by gray circles, and the data are from ATNF (ver. 1.70).

indicates its capability to detect weak sources but also raises the potential to update radiation theory in the future.

Acknowledgments

This work is supported by the National Natural Science Foundation of China grant (Nos. 12288102, 12041303, 12041304, 12273100, 11988101, T2241020), the National Key Research and Development Program of China (Nos. 2022YFC2205203 and 2022YFC2205202), and the Major Science and Technology Program of Xinjiang Uygur Autonomous Region (Nos. 2022A03013-3 and 2022A03013-4). D.L. is a New Cornerstone investigator. P.W. acknowledges support from the National Natural Science Foundation of China under grant U2031117, the Youth Innovation Promotion Association CAS (id. 2021055), NSFC 11988101, and the Cultivation Project for FAST Scientific Payoff and Research Achievement of CAMS-CAS. W.W.Z. is supported by National SKA Program of China No. 2020SKA0120200 and National Nature Science Foundation grant No. 11873067. S.J.D. is supported by the Guizhou Provincial Science and Technology Foundation (No. ZK[2022]304) and the Foundation of Education Bureau of Guizhou Province, China (grant No. KY (2020) 003). J.M.Y. is sponsored by the Natural Science Foundation of Xinjiang Uygur Autonomous Region (No. 2022D01D85), the Major Science and Technology Program of the Xinjiang Uygur Autonomous Region (2022A03013-2), the Tianchi Talent Project, the CAS Project for Young Scientists in Basic Research (YSBR-063), and the Tianshan Talents Program (2023TSYCTD0013).. This work made use of the data from FAST (Five-hundred-meter Aperture Spherical radio Telescope). FAST is a Chinese national mega-science facility, operated by National Astronomical Observatories, Chinese Academy of Sciences. We would like to thank the FAST CRAFTS group and XAO pulsar group for the provided data and helpful suggestions that led to significant improvement in our study. R.Y. is supported by the National Key Program for Science and Technology Research and Development No. 2022YFC2205201, the Major Science and Technology Program of Xinjiang Uygur Autonomous Region No. 2022A03013-2, and the open program of the Key Laboratory of Xinjiang Uygur Autonomous Region No. 2020D04049. This research is partly supported by the Operation, Maintenance and Upgrading Fund for Astronomical Telescopes and Facility Instruments, budgeted from the Ministry of Finance of China (MOF) and administrated by the CAS.

ORCID iDs

D. Zhao https://orcid.org/0009-0007-8062-1454
J. P. Yuan https://orcid.org/0000-0002-5381-6498
N. Wang https://orcid.org/0000-0002-9786-8548
D. Li https://orcid.org/0000-0003-3010-7661
P. Wang https://orcid.org/0000-0002-3386-7159
M. Y. Xue https://orcid.org/0000-0001-8018-1830
W. W. Zhu https://orcid.org/0000-0001-5105-4058
C. C. Miao https://orcid.org/0000-0002-9441-2190
W. M. Yan https://orcid.org/0000-0002-7662-3875
J. B. Wang https://orcid.org/0000-0001-9782-1603
J. M. Yao https://orcid.org/0000-0002-4997-045X
Q. D. Wu https://orcid.org/0000-0002-1495-4011
S. Q. Wang https://orcid.org/0000-0003-4498-6070
F. F. Kou https://orcid.org/0000-0002-0069-831X
S. J. Dang https://orcid.org/0000-0002-2060-5539
Y. Feng https://orcid.org/0000-0002-0475-7479
X. L. Miao https://orcid.org/0000-0003-1185-8937
L. Q. Meng https://orcid.org/0000-0002-2885-568X
M. Yuan https://orcid.org/0000-0003-1874-0800
C. H. Niu https://orcid.org/0000-0001-6651-7799
J. R. Niu https://orcid.org/0000-0001-8065-4191
L. Qian https://orcid.org/0000-0003-0597-0957
S. Wang https://orcid.org/0000-0002-1570-7485
Y. L. Yue https://orcid.org/0000-0003-4415-2148
R. S. Zhao https://orcid.org/0000-0002-1243-0476
X. Zhou https://orcid.org/0000-0003-4686-5977
L. Zhang https://orcid.org/0000-0001-8539-4237
Z. Y. Gan https://orcid.org/0000-0002-2431-1159
C. J. Wang https://orcid.org/0000-0003-4216-8090

References

Agazie, G., Alam, M. F., Anumarlapudi, A., et al. 2023a, ApJL, 951, L9
Agazie, G., Anumarlapudi, A., Archibald, A. M., et al. 2023b, ApJL, 951, L8
Agazie, G., Anumarlapudi, A., Archibald, A. M., et al. 2023c, ApJL, 951, L10
Agazie, G., Anumarlapudi, A., Archibald, A. M., et al. 2023d, ApJL, 951, L50
Agazie, G., Anumarlapudi, A., Archibald, A. M., et al. 2023e, ApJL, 956, L3
Agazie, G., Arzoumanian, Z., Baker, P. T., et al. 2023f, arXiv:2307.13797
Anumarlapudi, A., Swiggum, J. K., Kaplan, D. L., & Fichtenbauer, T. D. J. 2023, ApJ, 948, 32
Arons, J., & Scharlemann, E. T. 1979, ApJ, 231, 854
Belloni, D., & Schreiber, M. R. 2023, in Handbook of X-Ray and Gamma-Ray Astrophysics, ed. C. Bambi & A. Santangelo (Berlin: Springer), 129
Bhattacharyya, B., Gupta, Y., & Gil, J. 2010, MNRAS, 408, 407
Bhattacharya, D., & van den Heuvel, E. P. J. 1991, PhR, 203, 1
Bhattacharya, D., Wijers, R. A. M. J., Hartman, J. W., & Verbunt, F. 1992, A&A, 254, 198
Biggs, J. D. 1992, ApJ, 394, 574
Bisnovatyi-Kogan, G. S., & Komberg, B. V. 1974, SvA, 18, 217
Caleb, M., Heywood, I., Rajwade, K., et al. 2022, NatAs, 6, 828
Cameron, A. D., Li, D., Hobbs, G., et al. 2020, MNRAS, 495, 3515
Chen, H.-L., Chen, X., Tauris, T. M., & Han, Z. 2013, ApJ, 775, 27

Chen, K., & Ruderman, M. 1993, ApJ, 402, 264
Cordes, J. M., & Lazio, T. J. W. 2002, arXiv:astro-ph/0207156
Cruces, M., Champion, D. J., Li, D., et al. 2021, MNRAS, 508, 300
D'Antona, F., & Tailo, M. 2022, in Astrophysics and Space Science Library, ed. S. Bhattacharyya, A. Papitto, & D. Bhattacharya, Vol. 465 (Springer International Publishing), 201
Edwards, R. T., & Stappers, B. W. 2002, A&A, 393, 733
EPTA Collaboration, Antoniadis, J., Babak, S., et al. 2023a, A&A, 678, A48
EPTA Collaboration, InPTA Collaboration, Antoniadis, J., et al. 2023b, A&A, 678, A49
EPTA Collaboration, InPTA Collaboration, Antoniadis, J., et al. 2023c, A&A, 678, A50
Freire, P. C. C., & Ridolfi, A. 2018, MNRAS, 476, 4794
Goldreich, P., & Reisenegger, A. 1992, ApJ, 395, 250
Green, D. A. 2019, JApA, 40, 36
Han, J. L., Manchester, R. N., Lyne, A. G., Qiao, G. J., & van Straten, W. 2006, ApJ, 642, 868
Han, J. L., Wang, C., Wang, P. F., et al. 2021, RAA, 21, 107
Herfindal, J. L., & Rankin, J. M. 2007, MNRAS, 380, 430
Hobbs, G. B., Edwards, R. T., & Manchester, R. N. 2006, MNRAS, 369, 655
Hotan, A. W., van Straten, W., & Manchester, R. N. 2004, PASA, 21, 302
Jiang, L., Wang, N., Chen, W.-C., et al. 2020a, A&A, 633, A45
Jiang, P., Tang, N.-Y., Hou, L.-G., et al. 2020b, RAA, 20, 064
Kaplan, D. L., Swiggum, J. K., Fichtenbauer, T. D. J., & Vallisneri, M. 2018, ApJ, 855, 14
Kluzniak, W., Ruderman, M., Shaham, J., & Tavani, M. 1988, Natur, 334, 225
Lange, C., Camilo, F., Wex, N., et al. 2001, MNRAS, 326, 274
Lattimer, J. M., & Prakash, M. 2001, ApJ, 550, 426
Li, D., Wang, P., Qian, L., et al. 2018, IMMag, 19, 112
Lorimer, D. R., Bailes, M., Dewey, R. J., & Harrison, P. A. 1993, MNRAS, 263, 403
Lorimer, D. R., & Kramer, M. 2004, Handbook of Pulsar Astronomy, Vol. 4 (Cambridge: Cambridge Univ. Press)
Lorimer, D. R., & Kramer, M. 2012, Handbook of Pulsar Astronomy (Cambridge: Cambridge Univ. Press)
Lyne, A., Hobbs, G., Kramer, M., Stairs, I., & Stappers, B. 2010, Sci, 329, 408
Lyne, A. G., & Smith, F. G. 1968, Natur, 218, 124
Malov, I. F., & Malov, O. I. 2006, ARep, 50, 483
Manchester, R. N. 1974, ApJ, 188, 637
Manchester, R. N., Taylor, J. H., & Huguenin, G. R. 1975, ApJ, 196, 83
Miao, C. C., Zhu, W. W., Li, D., et al. 2023, MNRAS, 518, 1672
Nan, R. 2006, ScChG, 49, 129
Nan, R., Li, D., Jin, C., et al. 2011, IJMPD, 20, 989
Nice, D., Demorest, P., Stairs, I., et al., 2015 Tempo: Pulsar Timing Data Analysis, Astrophysics Source Code Library, ascl:1509.002
Olszanski, T., Rankin, J., Venkataraman, A., & Wahl, H. 2022, MNRAS, 517, 1189
Özel, F., & Freire, P. 2016, ARA&A, 54, 401
Pan, Z., Qian, L., Ma, X., et al. 2021, ApJL, 915, L28
Primak, N., Tiburzi, C., van Straten, W., Dyks, J., & Gulyaev, S. 2022, A&A, 657, A34
Qian, L., Pan, Z., et al. 2019, SCPMA, 62, 959508
Qian, L., Yao, R., Sun, J., et al. 2020, Innov, 1, 100053
Radhakrishnan, V., & Cooke, D. J. 1969, ApJL, 3, 225
Rankin, J. M. 1983, ApJ, 274, 333
Ransom, S., 2011 PRESTO: PulsaR Exploration and Search TOolkit, Astrophysics Source Code Library, ascl:1107.017
Reardon, D. J., Zic, A., Shannon, R. M., et al. 2023, ApJL, 951, L6
Ritchings, R. T. 1976, MNRAS, 176, 249
Ruderman, M. A., & Sutherland, P. G. 1975, ApJ, 196, 51
Stinebring, D. R., Cordes, J. M., Rankin, J. M., Weisberg, J. M., & Boriakoff, V. 1984, ApJS, 55, 247
Szary, A., Zhang, B., Melikidze, G. I., Gil, J., & Xu, R.-X. 2014, ApJ, 784, 59
Tauris, T. M., Kramer, M., Freire, P. C. C., et al. 2017, ApJ, 846, 170
Tauris, T. M., & Savonije, G. J. 1999, A&A, 350, 928
Thompson, D. J., Bailes, M., Bertsch, D. L., et al. 1999, ApJ, 516, 297
van den Heuvel, E. P. J., & van Paradijs, J. 1988, Natur, 334, 227
van Straten, W., & Bailes, M. 2011, PASA, 28, 1
Wang, Bo, Liu, Dongdong, Guo, Yunlang, et al. 2024, MNRAS, 532, 2196
Wang, N., Manchester, R. N., & Johnston, S. 2007, MNRAS, 377, 1383
Wang, P., Li, D., Clark, C. J., et al. 2021, SCPMA, 64, 129562
Wang, P. F., Han, J. L., Han, L., et al. 2020, A&A, 644, A73
Wang, P. F., Han, J. L., Xu, J., et al. 2023, RAA, 23, 104002
Wu, Q. D., Yuan, J. P., Wang, N., et al. 2023a, MNRAS, 522, 5152
Wu, Q. D., Wang, N., Yuan, J. P., et al. 2023b, ApJL, 958, L17
Wu, Q.-D., Zhi, Q.-J., Zhang, C.-M., Wang, D.-H., & Ye, C.-Q. 2020, RAA, 20, 188
Xie, M., Li, Y., Wang, Y., et al. 2022, arXiv:2203.05738
Xu, H., Chen, S., Guo, Y., et al. 2023, RAA, 23, 075024
Xu, H. W., Zhao, R. S., Gugercinoglu, Erbil, et al. 2024, APJ, 970, 148
Yao, J. M., Manchester, R. N., & Wang, N. 2017, ApJ, 835, 29
Zhang, B., Harding, A. K., & Muslimov, A. G. 2000, ApJL, 531, L135
Zhang, Lei, Li, Di, Hobbs, George, et al. 2019, APJ, 877, 55
Zhao, D., Wang, N., Yuan, J. P., et al. 2024, ApJL, 964, L7